

Ionized gas in the NGC 3077 galaxy

D. V. Oparin¹, O. V. Egorov^{2,1} and A.V. Moiseev^{1,2}

¹ Special Astrophysical Observatory, Russian Academy of Sciences, Nizhnij Arkhyz, 369167 Russia

² Sternberg Astronomical Institute, M.V.Lomonosov Moscow State University, Moscow, 119234 Russia

July 6, 2020/Revised: July 28, 2020/Accepted: July 28, 2020

Abstract. The nearby dwarf galaxy NGC 3077 is known for its peculiar morphology, which includes numerous dust lanes and emission-line regions. The interstellar medium in this galaxy is subject to several perturbing factors. These are primarily the central starburst and tidal structures in the M81 group. We present a comprehensive study of the state of ionization, kinematics, and chemical composition of ionized gas in NGC 3077, including both star-forming regions and diffuse ionized gas (DIG) at the periphery. We study gas motions in the H α line via high-resolution ($R \approx 15\,000$) 3D spectroscopy with the scanning Fabry-Perot interferometer installed into SCORPIO-2 instrument attached to the 6-m telescope of the Special Astrophysical Observatory of the Russian Academy of Sciences. Images in the main optical emission lines were acquired with MaNGaL photometer with a tunable filter at the 2.5-m telescope of the Caucasian Mountain Observatory of Sternberg Astronomical Institute of M.V. Lomonosov Moscow State University. We also used SCORPIO-2 to perform long-slit spectroscopy of the galaxy with a resolution of $R \approx 1\,000$. Our estimate of the gas metallicity, $Z = 0.6Z_{\odot}$, is significantly lower than the earlier determination, but agrees with the “luminosity–metallicity” relation. Spatially resolved diagnostic diagrams of the emission-line ratios do not show correlations between the gas ionization state and its velocity dispersion, and this is most likely due to strong ionization by young stars, whereas the contribution of shocks to the excitation of emission lines is less important. We also studied the locations of multicomponent H α profiles and provide arguments suggesting that they are mostly associated with individual kinematic components along the line of sight and not with expanding shells as it was believed earlier. We also observe there a combination of wind outflow from star-forming regions and accretion from interstellar gas clouds in the M81 group.

Key words. galaxies: dwarf—galaxies: ISM—galaxies: kinematics and dynamics—galaxies: starburst

1. INTRODUCTION

NGC 3077 is a dwarf galaxy, which is a member of the M81 group. Its absolute magnitude and adopted distance are $M_B = -17.62$ and 3.85 Mpc, respectively (Kaisina et al., 2012). NGC 3077 stands out among nearby galaxies by its peculiar morphology: numerous ionized-gas filaments and the associated dust lanes, which show up conspicuously in optical images (Fig. 1). HI line observations show that the galaxy is located near a giant tidal structure, which connects it to M81 and M82 (Yun et al., 1994; Sorgho et al., 2019), and the entire system is sometimes called the “M81 triplet” (de Blok et al., 2018). On the southern side of the galaxy a chain of clusters of blue stars and compact HII regions can be seen—it is the “Garland” tidal galaxy (Karachentsev et al., 1985; Makarova et al., 2002), which is located in a region of high HI density. The rate of ongoing star formation in NGC 3077 estimated from H α , luminosity and the HI mass are equal

to $SFR \approx 0.1 M_{\odot}/\text{yr}$ and $M_{\text{HI}} = 6.3 \times 10^8 M_{\odot}$, respectively (Karachentsev & Kaisin, 2007; Karachentsev et al., 2013), which is quite significant for a dwarf galaxy.

Martin (1998) used H α -echellegrams to demonstrate that NGC 3077 contains regions of broadening and bifurcation of emission lines interpreted as manifestations of several expanding shells of ionized gas. An estimate of virial velocities showed that their energy is insufficient for ejecting matter from the galaxy. The rotation curve of the galaxy was determined based on HI data and the rotation velocity was found to amount to 50 km s^{-1} . At the same time, H α observations show no signs of rotation (Epinat et al., 2008).

Ott et al. (2005) demonstrated the presence of a cluster of compact X-ray sources at the center of the galaxy, which are spatially associated with one of the expanding shells earlier discovered optically. It can be suggested that we are dealing with supernova remnants. The above authors point out that shells observed in emission lines are filled with optically thick gas. Note that unlike other seven dwarf starburst galaxies discussed in the above

Send offprint requests to: Dmitry Oparin e-mail: doparin2@gmail.com

paper NGC 3077 has close-to-solar metallicity (Storchi-Bergmann et al., 1994) and rather low X-ray brightness.

The diagrams of the flux ratios of bright optical emission lines ($[\text{O III}]/\text{H}\beta$, $[\text{N II}]/\text{H}\alpha$, $[\text{S II}]/\text{H}\alpha$)—the so-called BPT diagrams proposed in the classical paper by Baldwin, Phillips, & Terlevich (1981) and later further developed in Veilleux & Osterbrock (1987) are an important tool for studying the gas ionization state. The flux ratios of close lines, which depend only slightly on interstellar extinction, can be used to investigate various emission-line objects. These ratios allow regions of gas ionized by the radiation of OB stars be confidently distinguished from those where gas excitation is due mostly to other ionization sources (radiation of the active galactic nucleus, shocks). At the same time, these diagrams do not always allow one to separate the contribution of shock ionization from that of the radiation of old stars of the asymptotic giant branch or LINER-type galactic nuclei.

Hong et al. (2013) used optical narrow-band photometry acquired with the Hubble Space Telescope by Calzetti et al. (2004) to analyze the BPT diagrams of individual regions in NGC 3077 and demonstrated that shock ionization contributed to gas ionization in the regions located closer to the periphery of the galaxy. The above authors point out that weak manifestations of shocks in ionized gas may be difficult to discern in the presence of the powerful radiation of bright H II regions.

The contribution of shocks to the gas ionization state can be estimated by supplementing classical BPT diagrams with one additional parameter—line-of-sight velocity dispersion of ionized gas (σ) whose increase is associated with the increase of turbulent gas velocities behind the shock front. However, accurate measurements of σ require rather high spectroscopic resolution $R > 5000$ – 6000 . That is why in most of the surveys such approach is used to study objects with sufficiently high line-of-sight velocity dispersions (AGNs or starburst galaxies, where $\sigma > 100$ – 200 km s^{-1}), while being little used for studying dwarf galaxies and extended regions of diffuse ionized gas (DIG) with low surface brightness.

When studying such objects López-Cobá et al. (2017); Oparin & Moiseev (2018) used the line ratios determined with classical methods of integral-field spectroscopy combined with the data of observations made using Fabry-Perot interferometer (FPI) with sufficiently high spectroscopic resolution for estimating the velocity dispersion.

We report the results of a comprehensive analysis of the state of ionized gas in NGC 3077 based on new observational data: long-slit and 3D spectroscopy with the Fabry-Perot interferometer on the 6-m telescope of the Special Astrophysical Observatory of the Russian Academy of Sciences (SAO RAS) and narrow-band photometry with MaNGaL instrument attached to the 2.5-m telescope of the Caucasian Mountain Observatory of Sternberg Astronomical Institute of M.V. Lomonosov Moscow State University (CMO SAI MSU). We describe our observations and their reduction in Section 2. Section 3 describes the main observational results. In par-

ticular, Section 3.1 describes an analysis of the kinematics of ionized gas based on observations made with the FPI; Section 3.2 presents the results of our analysis of the emission spectrum of the galaxy and of the gas metallicity based on the data of long-slit spectroscopy; Section 3.3 considers the gas ionization state based on the data of narrow-band photometry performed with MaNGaL. Section 4 summarizes our conclusions.

2. OBSERVATIONS AND DATA REDUCTION

Table 1 lists the details of observations: the mode of observations, date, number and duration of exposures, seeing θ , spectral range $\Delta\lambda$ and spectral resolution $\delta\lambda$, and the image scale.

2.1. 3D spectroscopy with the scanning FPI

We investigated the kinematics of ionized gas in the $\text{H}\alpha$ emission line in the primary focus of the 6-m telescope of SAO RAS using SCORPIO-2 multimode focal reducer (Afanasiev & Moiseev, 2011) operating in the scanning Fabry-Perot interferometer (FPI) mode. The interferometer IFP751 provided a free spectral interval of $\Delta\lambda = 8.7 \text{ \AA}$ between neighboring interference orders with a scale of 0.22 \AA per channel. The operating spectral range in the vicinity of the redshifted $\text{H}\alpha$ was selected with the #77B narrow-band filter with a Central wavelength of $CWL = 6571 \text{ \AA}$. Scanning consisted of a sequence of 40 interferograms acquired with different spacings between the interferometer plates and uniformly filling the wavelength interval covered. The field of view had the size of $6'.1 \times 6'.1$ with a scale of $0''.7/\text{pixel}$. The result of reduction performed with the software described by Moiseev & Egorov (2008); Moiseev (2015) had the form of a data cube where each field-of-view pixel contained a 40-channel spectrum. Observations were made at two different orientations of the field of view of the instrument and the resulting data cubes were then coadded to remove parasitic ghosts (see Moiseev & Egorov, 2008).

2.2. Long-slit spectroscopy

We used the same SCORPIO-2 instrument attached to the 6-m telescope of SAO RAS in the long-slit spectroscopy mode (with the slit size of $6'.1 \times 1''$) to acquire spectra at two position angles ($PA = 234^\circ$ and 312°) passing through the cavity in the distribution of ionized gas in the $\text{H}\alpha$ line in the northern part of the central region of the galaxy. We show the location of the spectrograph slits in Fig. 1. We used a VPHG 1200@540 grating, which provided a spectral resolution of $\delta\lambda \approx 5 \text{ \AA}$ in the wavelength interval $\Delta\lambda = 3650$ – 7250 \AA .

We reduced observations in accordance with a standard procedure using an IDL software developed for reduction of long-slit data from SCORPIO-2. The principal reduction stages included bias subtraction, cosmic-ray hit removal, flatfielding, linearization, and subtraction

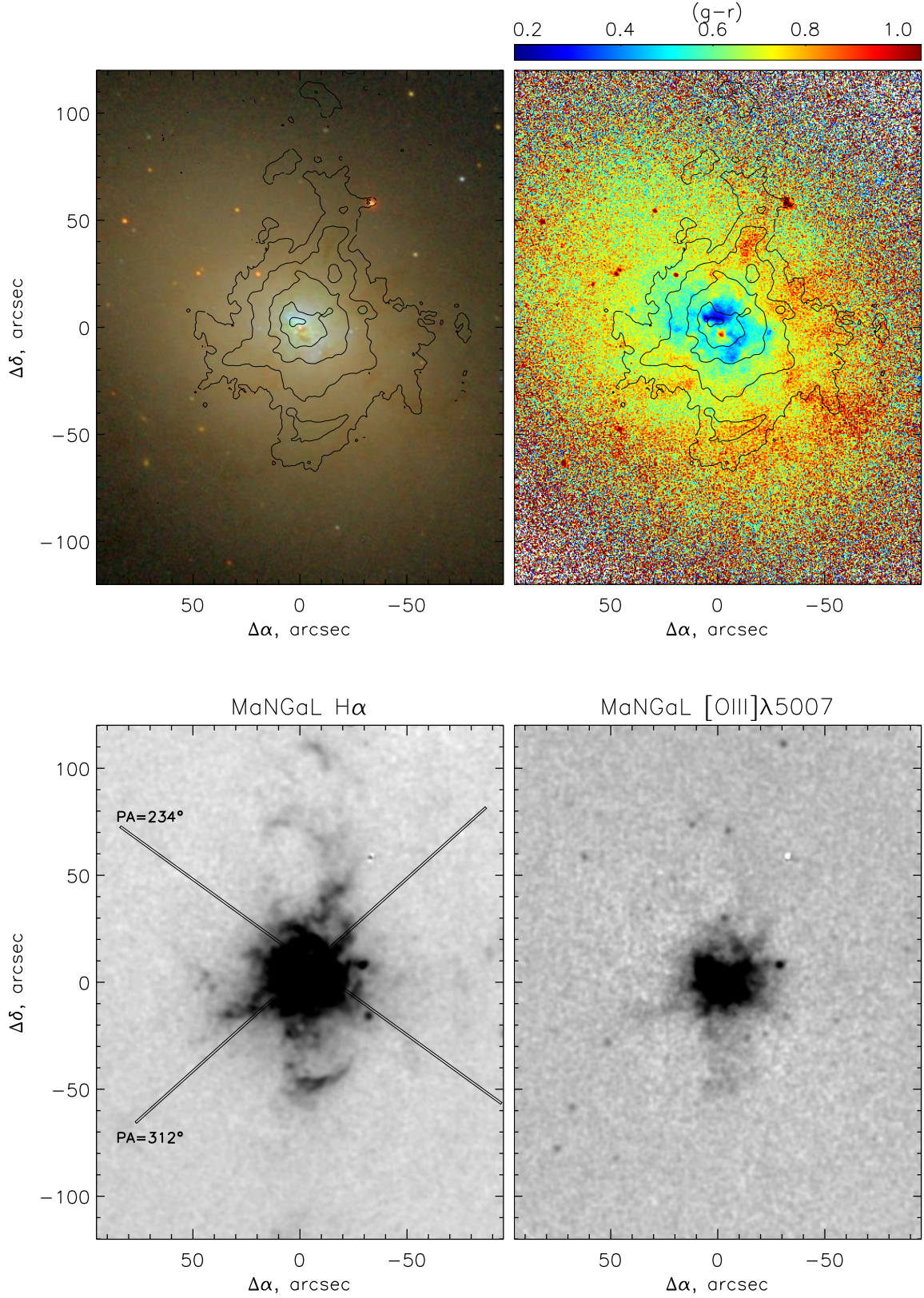


Fig. 1. The top row: composite color image of NGC 3077 adopted from SDSS DR15 sky survey (left) and $(g-r)$ color index map (right). Also shown are the H α -line contours based on the results of our FPI observations made with the 6-m telescope. The bottom rows: images acquired with MaNGaL on the 2.5-m telescope in the H α emission line with the positions of the SCORPIO-2 slits (left) and in the [O III] emission line (right).

Table 1. Log of observations of NGC 3077

Mode	Date	T_{exp} , s	θ , arcsec	$\Delta\lambda$, Å	$\delta\lambda$, Å	Scale, ''/px
LS $PA = 312$	Oct 11, 2013	6×1200	1.6	3650–7250	5.2	0.35
LS $PA = 234$	Feb 21, 2014	6×1200	2.8	3650–7250	5.2	0.35
FPI-1	Nov 09, 2013	40×300	2.0	8.7 in the vicinity of $H\alpha$	0.4	0.71
FPI-2	Nov 10, 2013	40×300	1.6	8.7 in the vicinity of $H\alpha$	0.4	0.71
MaNGaL	Apr 10, 2018	3×300	1.8	$H\alpha$	15	0.66
	Apr 10, 2018	6×300	1.8	[N II] λ 6583	15	0.66
	Apr 10, 2018	6×150	1.8	$H\alpha$ cont1	15	0.66
	Apr 10, 2018	5×150	1.8	$H\alpha$ cont2	15	0.66
	Apr 10, 2018	4×300	1.9	[S II] λ 6717	15	0.66
	Apr 10, 2018	4×300	1.9	[S II] λ 6731	15	0.66
	Apr 10, 2018	3×300	1.9	[S II] cont.	15	0.66
	Apr 10, 2018	7×300	2.0	[O III] λ 5007	15	0.66
	Apr 10, 2018	5×300	2.0	[O III] cont.	15	0.66

of the emission spectrum of the night sky. Wavelength calibration is performed using the He-Ne-Ar comparison spectrum taken on the same night. To take into account the spectral response of the instrument and transform the spectra to absolute energy units we used the spectrophotometric standards BD+28d4211 and BD+33d2642 whose spectra were acquired on the same night as those of NGC 3077 and at a similar zenith angle.

We used ULySS software suite¹ (Koleva et al., 2009) to model the spectrum of the underlying stellar population for each position along the slit and subtracted it from the acquired spectra. This procedure allowed us to analyze the emission spectrum of ionized gas in the galaxy. To measure emission-line fluxes, we fitted the line profile observed at each position along the slit by a single-component Gaussian using our IDL software based on MPFIT procedure (Markwardt, 2009). The flux errors presented below in the text and plots are the quadratic sums of errors due to noise and primary reduction and the error of the Gaussian fit.

All the fluxes that we report in this paper are corrected for interstellar extinction inside NGC 3077. We determined the color excess $E(B - V)$ for each region based on Balmer decrement ($H\alpha/H\beta$) and on a comparison with the theoretical flux ratio $H\alpha/H\beta = 2.86$ for $T_e = 10000$ K. To correct the fluxes for reddening we used the extinction curve of Cardelli et al. (1989) as parametrized in Fitzpatrick (1999).

2.3. Narrow-band photometry with MaNGaL

Narrow-band images of the galaxy in the emission lines [O III] λ 5007, $H\alpha$, [N II] λ 6583, [S II] λ 6717, 6731 were acquired with the MaNGaL (Mapper of Narrow Galaxy Lines) photometer with a tunable filter developed at SAO RAS (Moiseev et al., 2020) and attached to the Naysmith-2 focus of (Kornilov et al., 2014). The instrument is an afocal reducer with a low-resolution (interference order of about 20 at $H\alpha$ line) scanning piezoelectric FPI mounted in front of its camera in the converging beam. The width of

the instrumental contour (i.e., of the narrow-band filter) in the wavelength interval employed is $FWHM = 13 \pm 1$ Å. The central wavelength (CWL) can be set using CS-100 controller² with an accuracy of about 0.4 Å. A low-noise 1024×1024 iKon-M934 CCD was used as a detector. Observations were made in the instrumental binning mode (2×2) to reduce noise and readout time.

Unlike the classical FPI operating in a collimated beam, the adopted optical layout makes it possible to achieve a relatively large diameter of monochromatic beam (Jacquinot spots, see Jones et al., 2002). In our case the CWL of the FPI transmission varies by less than $\pm 0.5 FWHM$ throughout the entire $5'6 \times 5'6$ field of view. Therefore variations of CWL along the apparent NGC 3077 image can be neglected. Note also that according to our acquired velocity field (Fig. 3), Doppler variations of the emission-line wavelengths do not exceed 2–3 Å, i.e., they are small compared to the filter width.

During observations we successively accumulated the images in the process of the tune-up of the filter to the emission line (taking into account the average velocity of the galaxy and the heliocentric correction) and the continuum shifted by 30–50 Å. Observations performed in such series allow averaging the contribution from the variations of atmospheric transparency and seeing. The transmission peaks from neighboring interference orders were blocked using intermediate-band filters with a width of about 250 Å. Dedicated filters were used for observations in the [O III]+continuum, $H\alpha$ + [N II]+continuum, and [S II]+continuum lines. In the case of $H\alpha$ + [N II] lines the continuum images were taken in spectral bands on both sides of the line and then averaged, whereas in the case of the other lines the continuum images were taken only in one band.

Reduction of the acquired images differed little from standard reduction of direct images. After bias subtraction and flatfielding (illumination of the instrument by an incandescent lamp through an integrating sphere) the frames acquired in one spectral band were superposed,

¹ <http://ulyss.univ-lyon1.fr>

² All the FPIs and controllers used for observations are manufactured by IC Optical Systems Ltd, UK

and coadded with cosmic-ray hits removed in the process. Superposition was performed using reference stars. Continuum images multiplied by a close-to-unity coefficient determined so that the resulting flux from stellar images would be equal to zero were then subtracted from the images taken in emission lines. Continuum was observed at very close wavelengths and therefore the quality of its subtraction was appreciably higher than in the case of standard observations with 50–200 Å wide filters.

We performed absolute flux calibration of the images by observing spectrophotometric standards using the technique described in Moiseev et al. (2020).

The H α emission-line image (Fig. 1) shows practically all weak emission features seen in the deepest published images taken in this line with the 6-m telescope (Karachentsev & Kaisin, 2007), but with clearly better subtraction of foreground stars and stellar population of the galaxy. The [O III] image shows numerous compact objects, which are almost absent in H α . We consider them to be candidate planetary nebulae and supernova remnants. We will investigate them in a separate paper.

We used Astrometry.net³ (Lang et al., 2010) service to perform astrometric calibration of MaNGaL images and FPI data cube. This calibration allowed us to accurately compare the data of long-slit and field spectroscopy and tunable filter photometry. We then corrected the map of flux ratios in close $I([\text{N II}])/I(\text{H}\alpha)$ emission lines based on MaNGaL data for the effect of low spectral resolution in accordance with the equation reported in Moiseev et al. (2020).

2.4. Account of extinction and H β -line brightness map

For constructing the diagnostic diagrams separating the contributions from different ionization sources it is important to measure the $I([\text{O III}] \lambda 5007)/I(\text{H}\beta)$ emission-line ratio. We did not perform H β line observations with MaNGaL because the observed flux in this line is several times weaker than the H α flux and such observations would require too long exposures. Instead of this we tried to compute the H β brightness distribution based on an H α image and an extinction estimate based on SDSS DR9 photometry data using two different methods.

Method 1 interprets the decrease of the g -band brightness I at the given point relative to the mean brightness I_0 at the corresponding radius as dust extinction: $A_g = -2.5 \lg I/I_0$. We averaged the $I_0(r)$ profile over ellipses corresponding to the orientation of outer isophotes ($PA = 50^\circ$, $a/b = 0.85$). We masked the foreground stars, star-forming regions, and the most conspicuous dust lanes in the initial image. Because of the asymmetry in dust extinction we performed averaging separately on two sides from the major axis and then superposed the two halves to obtain the final A_g map. We interpreted the brightness excess relative to I_0 as the absence of extinction.

In method 2 the extinction estimate is based on the $(g-r)$ color-index map, which is used to construct the average radial profile of the $(g-r)_0$ color index of the stellar population obtained by averaging over the same elliptical rings as those used in method 1. We similarly masked the peculiar regions. We determined dust extinction as $A_g = 3.1E(g-r)$, where $E(g-r) = (g-r) - (g-r)_0$.

Both methods may yield biased result in extinction estimates. This is primarily due to the fact that dust in NGC 3077 has a complex and nonuniform distribution compared to stars, it shows individual filaments intricately associated with HII regions and diffuse gas. We therefore compared the maps of “photometric” extinction $A_{g,\text{phot}}$ obtained by our own method with spectroscopic $A_{g,\text{sp}}$ estimates along two available spectroscopic cross-cuts computed by the standard Balmer-decrement method as described above in Section 2.2. Our comparison showed that a correction factor $k = A_{g,\text{sp}} - A_{g,\text{phot}}$ has to be introduced. The factor k so determined also takes in to account the foreground line-of-sight extinction in the Milky Way. However, method 1 better describes the variations of extinction observed along the spectrograph slit and the correction factor is smaller. We therefore computed the H β brightness map using Method 1.

3. RESULTS OF OBSERVATIONS

3.1. Analysis of the kinematics in the H α line

Emission-line profiles of ionized gas observed with FPI usually fit quite well the Voigt function (Moiseev & Egorov, 2008; Moiseev, 2015). The result of a fit of individual spectra in the data cube were used to construct galaxy images in the emission line and in the continuum, as well as the maps of radial velocity and velocity dispersion σ free from instrumental broadening. The bottom panels of Fig. 2 show the maps of the distribution of radial velocities and velocity dispersion σ obtained by fitting a single-component Voigt profile to the data cube (the top panels show the distribution of H α surface brightness according to MaNGaL observations in the same scale).

Although the radial-velocity map of the galaxy shows a certain ($\approx 20 \text{ km s}^{-1}$) difference in the West to East direction, it does not exhibit a conspicuous rotational pattern, no rotation axis can be found, and the circular motion cannot be properly fitted by a well-defined model. This is consistent with the results of Epinat et al. (2008). The velocity dispersion estimates that we inferred from H α data mostly do not exceed 20–30 km s^{-1} , amounting to 35–60 km s^{-1} in some contact regions. In particular, some of these high-dispersion regions coincide with compact X-ray sources from Ott et al. (2005).

An analysis of the H α data cube of NGC 3077 revealed numerous regions exhibiting a complex structure of the emission-line profile: asymmetry, splitting into two or more components (see examples of the profile decomposition in Fig. 2). The very center of the galaxy exhibits a conspicuous single-component H α profile. At the same

³ <http://astrometry.net>

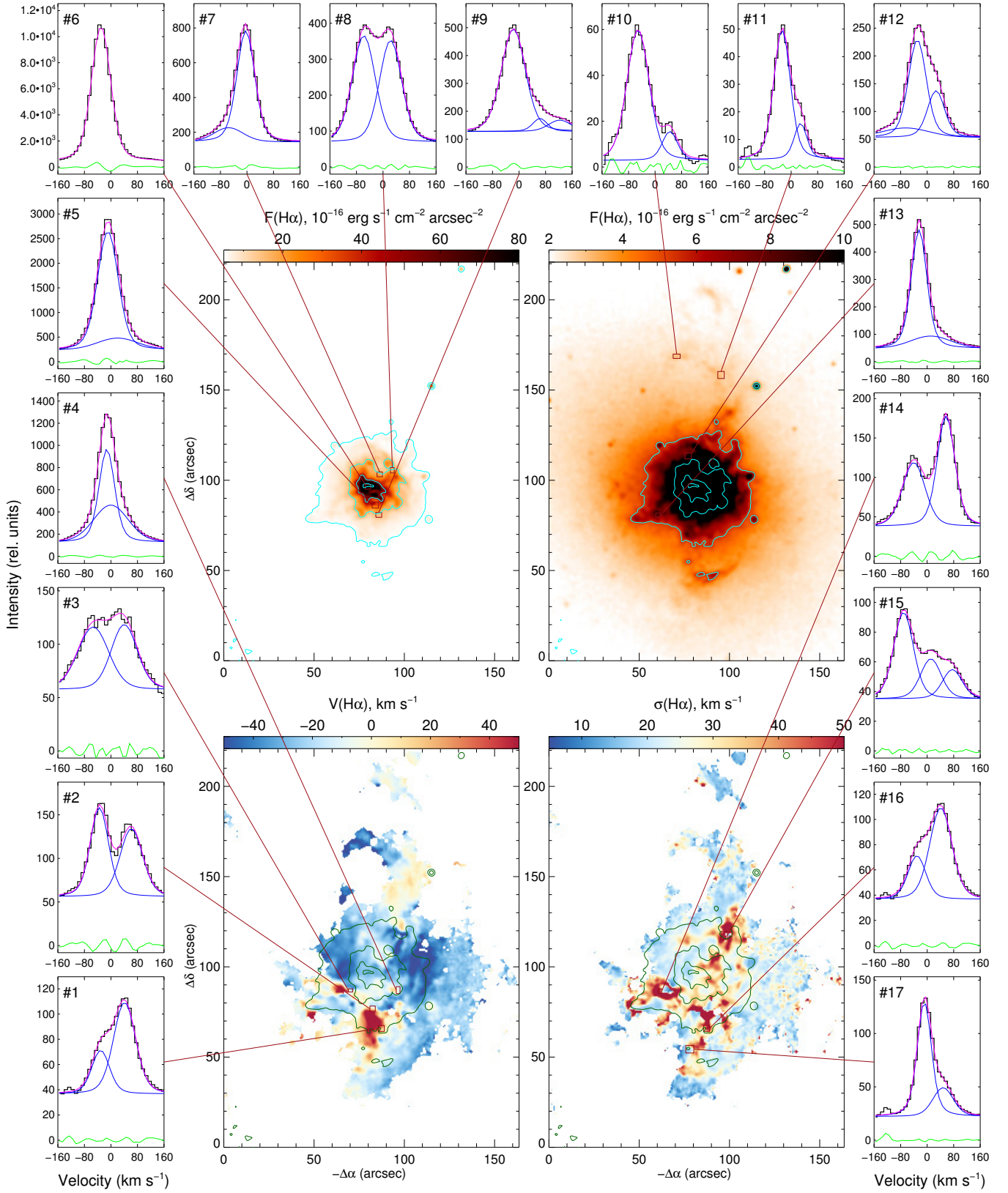


Fig. 2. Example of observed $H\alpha$ profiles and the result of their decomposition into 1–3 Voigt functions (the corresponding profiles are shown in blue, whereas the green plots show the residual obtained by subtracting these profiles from the observed spectrum). The profiles are obtained by integrating over the rectangular areas indicated in the images. The upper row of images demonstrates the $H\alpha$ flux distribution for different intensity levels. The lower row shows the fields of line-of-sight velocities (left) and velocity dispersion (right) obtained by fitting the observed profiles by a single-component Voigt function. The isophotes correspond to the $H\alpha$ brightness $(0.2, 0.5, 1.6, 4.9, 14.6) \times 10^{-16} \text{ erg s}^{-1} \text{ cm}^{-2} \text{ arcsec}^{-2}$

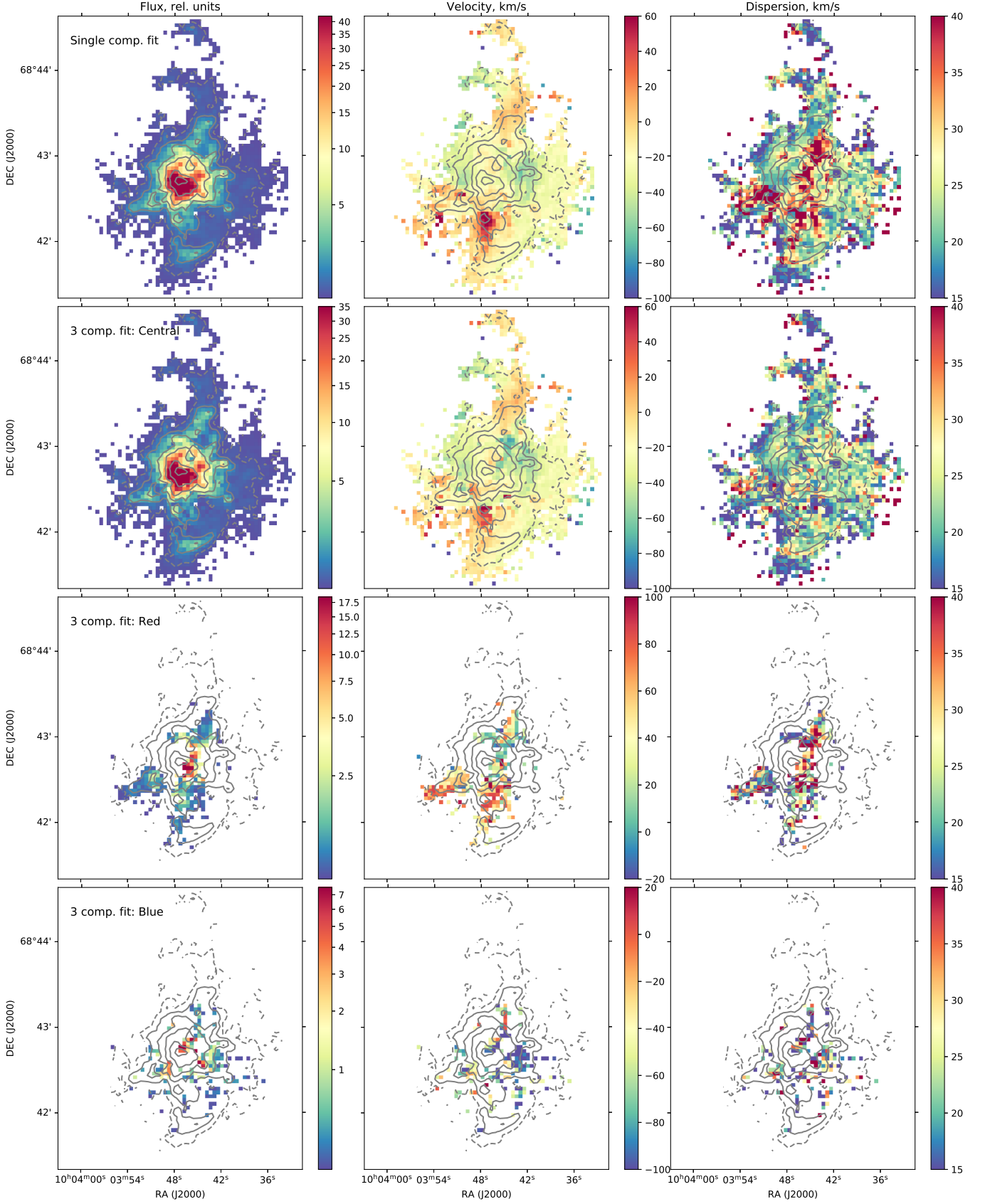


Fig. 3. Results of the decomposition of the H α FPI data cube for NGC 3077 into one and three kinematically decoupled components. Left to right—H α flux, line-of-sight velocity, and velocity dispersion maps. The top panels are obtained by decomposing via a single-component Voigt profile, whereas the three bottom panels contain information about the central and red- and blueshifted components in the case of the three-components decomposition.

time, complex multicomponent profiles are found practically throughout the entire galaxy outside the brightest H II region. In particular, in all regions with high velocity dispersion inferred from a single-component fit H α profiles are observed that clearly split into two or three components (see, e.g., profiles #14–17 in Fig. 2). A similar pattern is also observed in regions with the largest radial velocities (profiles #1–4).

To assess the behavior of gas motions in the galaxy, we tried to decompose the H α profiles into kinematically decoupled components throughout the entire data cube and follow the space distribution of each component. To this end, we fitted the H α profile in each spatial element of the data cube (prebinned with a 4-pixel bin size to increase the signal-to-noise ratio) by 1–3 components. We performed the procedure iteratively starting with the smallest number of components and adding the next component in the case if the residual from the subtraction of the model exceeds the noise level by a factor of three. We adjusted the number of components manually in some regions based on the results of a visual inspection of the results of automatic analysis. We then identified the “central”, “blue”, and “red” components (in accordance with their radial velocities) and analyzed the space distribution of their properties. In the case of a two-component profile we considered the brightest peak to be the “central” component. The results are presented in Fig. 3, the top panel shows the previous result of fitting by a single component for comparison.

The maps of kinematically distinct components reveal that practically all high-dispersion regions in Fig. 2 and in the top panel in Fig. 3 show a (mostly) redshifted or a blueshifted component. The velocity dispersion of the central component practically coincides with that of unperturbed regions of the galaxy. Note also that the locations of the red- and blueshifted components coincide with the dust lanes seen in SDSS images and also with the superbubbles found based on the data of echelle spectra (Martin, 1998).

The complex structure of the line profile makes it difficult to uniquely separate the components and construct their spatial distribution preventing bona fide reconstruction of the 3D structure of the ionized gas. However, we do not observe the line-of-sight velocity distribution pattern characteristic of expanding supershells, where the velocity difference between the components is maximal at the center of the bubble and decreases toward the edges. At the same time, we cannot rule out the existence of compact shell-like structures, like, e.g., those described in Egorov et al. (2014, 2018), or the existence of expanding superbubbles in significantly nonuniform medium (Lozinskaya et al., 2003; Egorov et al., 2010).

Note also that some profiles shown in Fig. 3 (#5, 7, 12, 13), exhibit a broad component with low brightness, which can actually be identified in a substantial part of the galaxy, but its contribution was not taken into account in Fig. 3. Hence we may be dealing with yet another low-brightness component with $\sigma > 100\text{--}150\text{ km s}^{-1}$. The ve-

locity dispersion estimate mentioned above was obtained assuming that $FWHM$ is comparable to or exceeds the working range of the FPI and therefore cannot be determined. Note that Bresolin et al. (2020) recently demonstrated conclusively the presence of broad components in several giant star-forming regions in the M 101 galaxy. The widths of these components measured by the zero intensity level ($FWZI$) could be as large as $750\text{--}1300\text{ km s}^{-1}$, implying a velocity dispersion $\sigma = 100\text{--}200\text{ km s}^{-1}$ (assuming that $FWHM \approx FWZI/3$). The presence of such a broad component in regions of ongoing star formation can be associated with the effect that winds from massive stars have on the surrounding molecular clouds.

3.2. Analysis of long-slit spectra

Fig. 4 shows the results of the analysis of the flux ratio ratios in some emission lines and the metallicity distribution along the spectrograph slit whose location is indicated by the horizontal line in the top panel.

Until recently, the metallicity of the interstellar medium in NGC 3077 was studied only by Storchi-Bergmann et al. (1994) based on the optical spectrum of the central part of the galaxy in a large aperture. They estimated the oxygen abundance, which serves as an indicator of the gas metallicity in the interstellar medium, to be $12 + \log(\text{O}/\text{H}) = 8.64$. Such an estimate is indicative of the solar abundance of heavy elements, which is not typical of dwarf galaxies of such luminosity (the galaxy deviates from the “luminosity–metallicity” relation Pilyugin et al., 2004). Calzetti et al. (2004) used the same spectrum to infer an even higher abundance of $12 + \log(\text{O}/\text{H}) = 8.9$. Such a significant difference is primarily due to the fact that the authors of the two studies used different families of strong-line methods (calibrated by H II regions with bona fide estimates of electron temperature T_e and from photoionization models), which can result in discrepancies of up to 0.6 dex (see, e.g., Kewley & Ellison, 2008). Our long-slit spectroscopy data allow us not only to refine the gas metallicity in NGC 3077, but also to investigate its variation along the slits.

We used two empirical methods to estimate the relative oxygen abundance $12 + \log(\text{O}/\text{H})$: O3N2 (Marino et al., 2013) and S (Pilyugin & Grebel, 2016), which are based on the bright emission-line ratios $[\text{O III}]/\text{H}\beta$, $[\text{N II}]/\text{H}\alpha$ and $[\text{S II}]/\text{H}\alpha$ (only in the case of the S method). Both methods are calibrated by H II regions with available bona fide measurements of electron temperature T_e and metallicity made using the T_e method. We excluded from our analysis the pixels that do not fall within the H II regions in BPT diagrams (see below) or having equivalent widths $EW(\text{H}\alpha) < 6\text{ \AA}$. It follows from Fig. 4 that both methods yield similar values with no signs of metallicity gradient, but with small variations, which can be due to the variation of the ionization parameter caused by the contribution of DIG or just by the error of the methods, which amounts to about 0.10–0.15 dex.

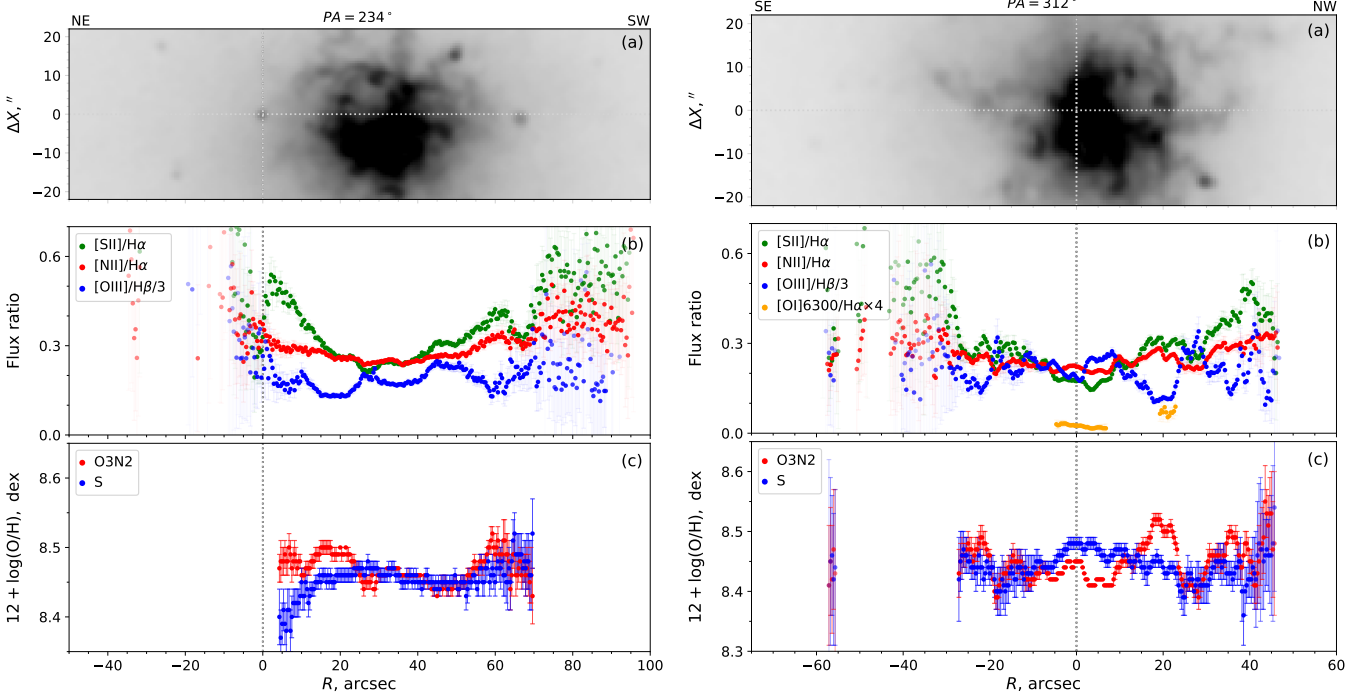


Fig. 4. Results of an analysis of the emission spectrum acquired with the spectrograph slit at $PA = 234^\circ$ (left) and $PA = 312^\circ$ (right). The panels—top to bottom—show: (a) $H\alpha$ map of the galaxy obtained with MaNGaL (the horizontal line corresponds to the alignment of the spectrograph slit); (b) the distribution of line flux ratios; (c) the distribution of the relative oxygen abundance $12 + \log(O/H)$ estimated using two empirical methods.

The estimates determined by applying the two methods to the integrated spectrum of the central part (-5 to $+7$ arcsec from the slit center along the slit direction for $PA = 312^\circ$) are equal to $12 + \log(O/H)_{O3N2} = 8.43 \pm 0.02$ and $12 + \log(O/H)_S = 8.47 \pm 0.03$ (the quoted errors do not include the errors of the methods). In this region the signal-to-noise ratio in the blue part of the spectrum was sufficient for including the $[OII] \lambda 3727/H\beta$ ratio into the analysis. We added this ratio to our metallicity analysis and used the R-method from Pilyugin & Grebel (2016) to obtain the estimate $12 + \log(O/H)_R = 8.49 \pm 0.05$, which is consistent with the results mentioned above. Thus unlike what was believed before the gas metallicity in the galaxy is, according to our measurements, significantly lower than the solar value and is equal to $Z = 0.6Z_\odot$. We found no significant variations of the oxygen abundance along the slit. However, as we point out in Section 3.3 below, more enriched gas associated with the tidal flow from M 81, can be observed at the periphery of the galaxy. Our estimate of the gas metallicity agrees well with the “luminosity–metallicity” relation from Pilyugin et al. (2004) for the adopted NGC 3077 absolute magnitude of $M_B = -17.62$.

Fig. 5 shows the diagnostic diagrams $[OIII]/H\beta$ vs $[NII]/H\alpha$, $[SII]/H\alpha$, and $[OI]/H\alpha$ based on the results of spectroscopic observations. The top panels show color-coded $H\alpha$ surface brightness; the four lines indicate the position of the curve from Kewley et al. (2001) that separates the domains where emission can be explained by

photoionization from the domains with another excitation mechanism (AGN, shocks). The gray line in the left-hand panel from Kauffmann et al. (2003) separates H II regions from regions with a composite ionization mechanism. The straight line in the $[OIII]/H\beta$ – $[SII]/H\alpha$ diagram from Kewley et al. (2006) separates the Seyfert and LINER domains. Also shown in the figure are the shock models adopted from Allen et al. (2008) for the case of the metallicity of $Z = 0.6Z_\odot$ corresponding to our estimate for NGC 3077. Various color curves correspond to models with different shock velocities. Note that the top panels show the models with the precursor contribution, whereas the bottom panels show the models including the contribution from shocks exclusively. It follows from the diagrams that the entire bright emission is associated with photoionization by massive stars in star-forming regions, whereas the domain of composite excitation is populated only by the points corresponding to low surface brightness DIG. As is evident from a comparison of diagnostic diagrams with the models of shocks, their effect can explain the ionization of low surface brightness regions (the discrepancy between shock models and observations in the case of $[OI]/H\alpha$ is due to the lack of $[OI]$ line data for DIG regions). Note that the shock models without the photoionization precursor are worse to explaining observational data. This fact leads us to conclude that the leakage of ionizing photons from star-forming regions play an essential role in the ionization of DIG in the regions located on the slit. In this case shocks did not play an important

role in the ionization of observed bright regions of ionized gas including extended filaments and superbubbles.

The bottom panels in Fig. 5 show the BPT- σ diagrams with color coded line-of-sight velocity dispersion (determined from FPI spectra as a result of a single-component profile decomposition) measured along the spectrograph slit. As is evident from the data shown in the diagrams, in the case of NGC 3077 regions of high velocity dispersion are associated with star-forming regions and not with shocks. However, the [SII]/H α diagram shows a small shift of high-dispersion regions toward higher line ratios.

3.3. BPT diagrams based on narrow-band photometry

The BPT diagrams based on the data of long-slit spectroscopy cannot describe the state of ionized gas throughout the entire galaxy and therefore we reconstruct the emission-line ratios from the results of photometry with a tunable filter.

Fig. 6 shows the diagnostic BPT diagrams based on the [O III]/H β , [N II]/H α , and [S II]/H α line ratios obtained via mapping with MaNGaL. The color coding corresponds to line-of-sight velocity dispersion estimates inferred from FPI data. The figure shows three sets of diagrams for different regions of the galaxy (see below). The right-hand panels show the maps of line-of-sight velocity dispersion included into each set. We adopted the parametrization of the curves that separate regions with different type of ionization (photoionization regions—H II, objects with composite ionization type—Comp., active Seyfert galaxies—Seyfert, and LINER type objects) from Kewley et al. (2006). The color lines, like in Fig. 5, correspond to shock models for different velocities adopted from (Allen et al., 2008), but the bottom panel shows the values for solar metallicity (in the top panel, for $Z = 0.6Z_{\odot}$). The top panel in Fig. 6 shows the diagrams obtained for the entire galaxy based on the data with original pixel size. The absolute majority of the data points in the diagrams lies in the domains characteristic for photoionization by the radiation of OB stars and show no appreciable contribution from shock ionization. Only a small fraction of the data points is located in regions of composite ionization. This result agrees with the results of our long-slit observations, however, compared to the diagrams reported by Calzetti et al. (2004); Hong et al. (2013) our data points are shifted downward. In our opinion, this is due to the specificities of the technique of the photometry in narrow- and intermediate-band filters used on the Hubble Space Telescope. In particular, in HST observations the contribution of continuum radiation of the stellar population was taken into account by subtracting from [O III] and H β line data the F547M-band frames whose effective wavelength is rather far from the above lines. The technique of accounting for the contribution of the continuum based on two images taken at close wavelengths that we employed in our observations with a tunable filter allowed us to more accurately estimate the fluxes in emission lines.

Furthermore, our spectra show that the effect of the absorption line from stellar population is quite significant in the region of the H β line. This effect is difficult to properly account for in filter frames and that must explain the overestimated [O III]/H β ratios reported in the above papers. Our technique for computing the distribution of the H β flux from the H α image using the extinction map is free from this disadvantage as confirmed by the agreement between the line ratios based on SCORPIO-2 data, which take into account the model of the stellar population, and the ratios based on MaNGaL photometry.

The surface brightness in the [O III] λ 5007 line in outer regions of the galaxy is appreciably lower than the surface brightness in [N II] and [S II] lines, which is typical for DIG. Therefore, the outer regions of the galaxy, where brightness in the oxygen line is lower than the noise level but the signal is quite appreciable in the nitrogen and sulfur lines, are excluded from the analysis of BPT diagrams. To overcome this limitation, we artificially fixed the [O III] λ 5007 line flux at the level equal to the standard deviation of noise level for the regions where the [N II] and [S II] are reliably detected, and [O III] line is undetected. Thus the fixed [O III] line flux is equal to its upper boundary. Such a procedure allows us to follow the variations of the excitation mechanism by analyzing the variations of the [N II]/H α and [S II]/H α ratios on the BPT diagrams including the regions with insufficiently high S/N ratios in the [O III] λ 5007 line. Fig. 6 shows the BPT diagrams and the map of velocity dispersion for “inner” regions of the galaxy where [O III] λ 5007 line is securely detected (the middle panel), and also for outer regions where $S/N \leq 3$ (the bottom panel).

As is evident from the middle panel in Fig. 6, emission in the central part of the NGC 3077 can be fully explained by photoionization by OB stars, and this also applies to regions with high velocity dispersion. On the other hand, the outer parts of the galaxy (the bottom panels) show a well-defined trend toward the right-hand part of the BPT diagram, beyond the region of photoionization by young stars, which lies below the demarcation line between the Seyfert and LINER domains. Our adopted [O III] λ 5007 line flux in outer regions is an upper estimate and therefore in reality the data points on the BPT diagram should be located no higher than they are located in Fig. 6.

Note that the observed position in BPT diagrams in the LINER domain can be explained quite well by shock models (Allen et al., 2008) both in the case of the metallicity close to our estimate for NGC 3077 (see models in the top panel) and for $Z = Z_{\odot}$ (see the bottom panel). Adding photoionization precursor to these models allows to even better explain the flux distribution in the left-hand panel, but the agreement is significantly worse for [S II]/H α , and this fact is indicative of a significant contribution of shocks to ionization in outer regions. No correlation with the velocity dispersion of ionized gas is observed in this case. For outer regions the positions of data points in the BPT diagram can be better reproduced in the case of significantly lower shock velocities if shocks propagate through

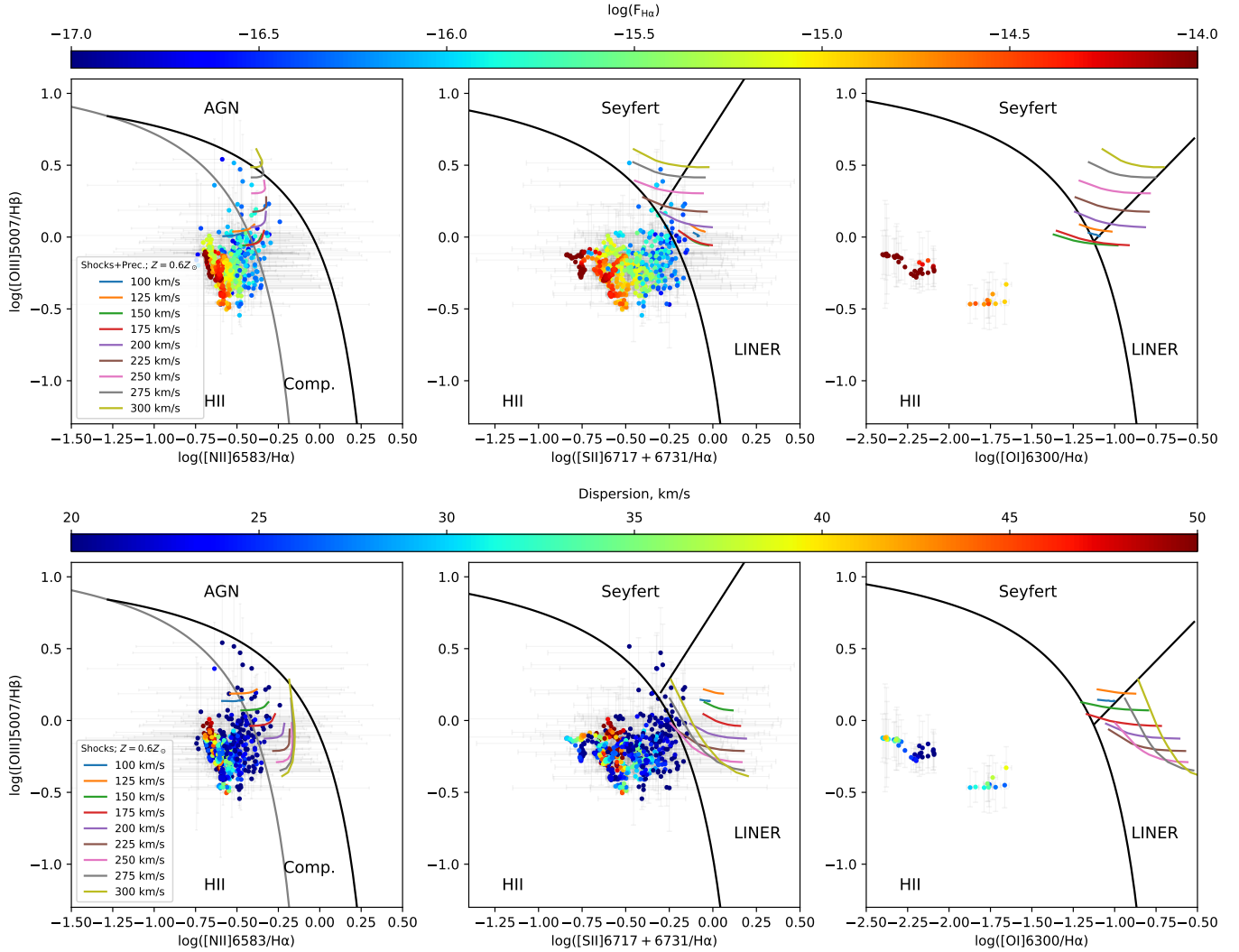


Fig. 5. BPT diagrams based on spectroscopic observations. Color bar corresponds to the logarithm of the $H\alpha$ surface brightness (the top panel) and line-of-sight velocity dispersion (the bottom panel). The black and gray curves that separate star-forming regions, composite ionization mechanism, and LINERS are adopted from Kewley et al. (2001) and Kauffmann et al. (2003). The diagonal line that separates the Seyfert and LINERs regions is adopted from Kewley et al. (2006). The color lines correspond to shock models in accordance with Allen et al. (2008) for different velocities for the metallicity of $Z = 0.6Z_{\odot}$. The top panels show the models with the precursor and the bottom panels show the models with shocks exclusively.

a medium with solar content of heavy elements than if we assume the metallicity at the periphery to be equal to our estimate for the central part based on long-slit spectroscopy.

An analysis of the BPT diagram for the periphery of NGC 3077 suggests that we observe there a significant contribution of shocks propagating through a medium with possibly more metal-rich gas compared to the central part of the galaxy. Such a pattern can be explained both by the interaction between the galaxy and a giant tidal HI structure, and by manifestations of the galactic wind ejecting metal-enriched to the periphery. Both processes can be responsible for shocks and, possibly, for higher metallicity of gas at the periphery. However, in the case of the external accretion of gas clouds we can hardly expect high-velocity shocks: according to our analysis of the maps published in

Walter et al. (2002, 2008), the line-of-sight velocity of HI clouds is of about $-5 \pm 15 \text{ km s}^{-1}$, which agrees well with the systemic velocity of NGC 3077. The hypothesis that mutual motions occur in the sky plane is too daring. On the other hand, in the case of significant mass outflow we could expect appreciable manifestations of shocks toward the center of the galaxy. However, BPT diagrams in the central part of the galaxy show no signs of shocks and the main kinematically distinct supersonic gas motions are observed along large-scale gas-and-dust filaments or are associated with local X-ray sources (supernovae) and not with the large-scale gas outflow from the galaxy. We can conclude that photoionization by the UV radiation of young stars in the central part of NGC 3077 is evidently the main contributor to gas ionization compared to shocks. Note that such a pattern is typical for known cases of galactic

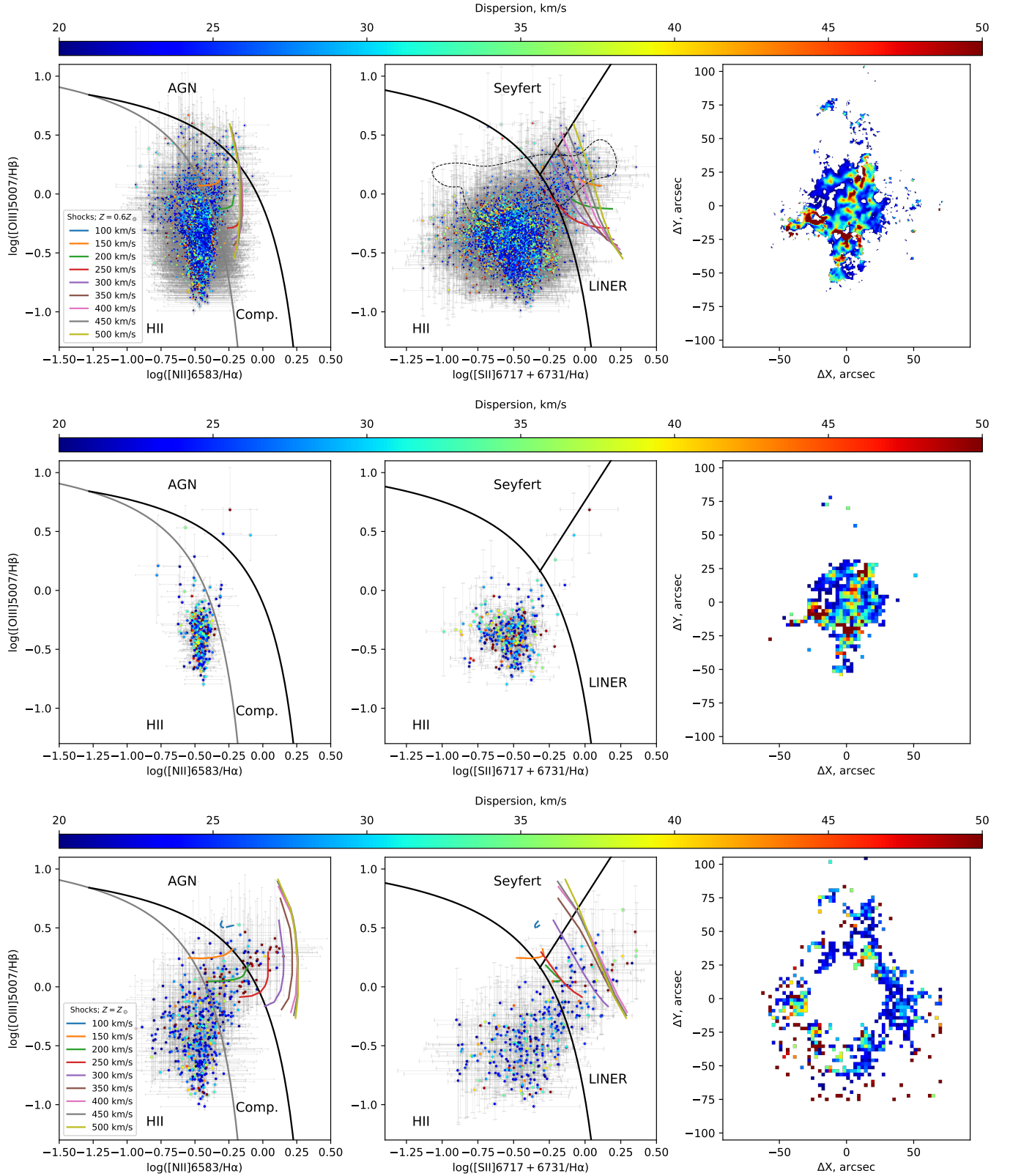


Fig. 6. The BPT diagrams based on the results of observations with a tunable filter. The top panels show the result obtained for the entire galaxy with the original pixel size. The middle and bottom panels show the diagrams for the inner and outer regions with binning=4. The colors are used to code the $H\alpha$ velocity dispersion, the right-hand panels show the corresponding velocity dispersion maps for each set of regions. The curves separating the domains of the diagram with different gas ionization mechanisms are similar to those shown in Fig. 5. The color curves correspond to shock models in accordance with Allen et al. (2008) for different velocities and metallicities $Z = 0.6Z_{\odot}$ (the top panels) and $Z = Z_{\odot}$ (the bottom panels). The dashed line in the top middle panel outlines the domain of observed line flux ratios according to Hong et al. (2013).

wind: the $I(\text{[N II]})/I(\text{H}\alpha)$ ratio corresponds to its value for H II regions in the disk of the galaxy, but increases toward the periphery with increasing distance from central star-forming regions (see, e.g., López-Cobá et al. 2017, 2019). Note that the presence of a broad low-contrast component in the $\text{H}\alpha$ line in central regions of the galaxy is indicative of the outflow of high-velocity gas from star-forming regions.

Despite the manifestations of gas outflows mentioned above we see no appreciable correlation between the line ratio and σ observed in dwarf galaxies with ongoing star formation, primarily in those with galactic wind (López-Cobá et al., 2017; Oparin & Moiseev, 2018). This must be due to the fact that what we see along the line of sight is a mix of several emission components: gas in star-forming regions, gas flowing out from the disk, and accretion flows toward the disk. We observe the multicomponent structure of profiles in FPI data. However, we so far could not uniquely associate the velocity dispersion of each component with its individual diagnostic line ratio, because the observed line ratios were measured in low-resolution spectra. Perhaps it will be possible to do it later using additional spectroscopic data and new algorithms of profile decomposition.

4. CONCLUSIONS

We used observations made with the 6-m telescope of SAO RAS and 2.5-m telescope of Caucasian Mountain Observatory of Sternberg Astronomical Institute of M.V. Lomonosov Moscow State University using the methods of long-slit and 3D spectroscopy and narrow-band photometry in emission lines to investigate ionized gas in the NGC 3077 galaxy.

Observations with a scanning FPI allowed us to map the distributions of line-of-sight velocities and velocity dispersion of ionized gas with high spatial resolution. We used the results of long-slit spectroscopy to estimate the relative oxygen abundance in the interstellar medium of the central region of the galaxy, $12 + \log(\text{O}/\text{H}) = 8.43\text{--}8.49$ ($Z \approx 0.6Z_{\odot}$), which is significantly lower than the earlier estimate $Z = Z_{\odot}$ and agrees with the expected value for NGC 3077 given its luminosity. We detected no radial metallicity gradient. The diagrams of the emission-line ratios based on the data of long-slit spectroscopy and photometry with a tunable filter allowed us to refine the results earlier published by Hong et al. (2013). The good agreement between the BPT diagrams that we obtained using two different methods shows that the use of photometry with a tunable filter to study the ionization state can be a good alternative to classical spectroscopic methods for investigating the sources of gas ionization in extended objects including objects with low surface brightness.

Despite the presence in NGC 3077 of some regions with relatively high line-of-sight velocity dispersion of ionized gas—up to $\sigma \approx 60 \text{ km s}^{-1}$, there is no correlation between the location of points in the BPT diagram and velocity dispersion σ , like in the case of the dwarf galaxy

VII Zw 403 (Oparin & Moiseev, 2018). In the central parts of NGC 3077 no appreciable contribution of shocks to gas ionization can be seen. This must be due to the strong photoionization just in star-forming regions: a weak contribution of shocks to the excitation of [N II] and [S II] can possibly not show up in the wings of the bright $\text{H}\alpha$, line shifting the [N II]/ $\text{H}\alpha$ and [S II]/ $\text{H}\alpha$ ratios leftward in the BPT diagram. In this case high velocity dispersion in $\text{H}\alpha$ can be explained by the superposition of several components along the line of sight. The decomposition of the data cube obtained with FPI in the $\text{H}\alpha$, line allowed us to investigate the distribution of at least three kinematically distinct components in the galaxy. The results showed in many regions the contribution of the broad ($\sigma > 100 \text{ km s}^{-1}$) low surface brightness component, which is probably associated with the manifestation of winds from massive stars in star-forming regions.

The inferred picture of the distribution of line-of-sight velocities suggests that a part of the regions with a conspicuous multicomponent profile that were earlier found based on the data of echelle spectra (Martin, 1998) are separate kinematic components rather than single expanding superbubbles, and this conclusion is also confirmed by the fact that some of them coincide with the dust lanes in optical images. In our opinion, we are dealing with the infall of cold gas from a tidal structure onto the disk of the galaxy. This infall triggers star formation at the center of NGC 3077.

Acknowledgements. We are grateful to A. M. Tatarnikov and N. I. Shatskii for organizing observations at Caucasian Mountain Observatory of Sternberg Astronomical Institute; to V. L. Afanasiev and A. N. Burenkov for conducting observations with the 6-m telescope of the Special Astrophysical Observatory of the Russian Academy of Sciences, and to T. A. Lozinskaya for her assistance with data acquisition and discussion of the work. This research has made use of the NASA/IPAC Extragalactic Database (NED), which is operated by the Jet Propulsion Laboratory, California Institute of Technology, under contract with the National Aeronautics and Space Administration and public data of the SDSS survey (site <http://www.sdss3.org/>, which is funded by the Alfred P. Sloan Foundation, SDSS Participating Institutions, National Science Foundation, the US Department of Energy, the National Aeronautics and Space Administration (NASA), the Japanese Monbukagakusho, the Max Planck Society, and the Higher Education Funding Council for England.

FUNDING

This work was supported by the Russian Science Foundation (project no. 17-12-01335 “Ionized gas in galactic disks and beyond the optical radius”). Observations on the telescopes of SAO RAS are carried out with the support of the Ministry of Science and Higher Education of the Russian Federation (contract No. 05.619.21.0016, project ID RFMEFI61919X0016).

References

- Afanasiev, V. L. & Moiseev, A. V. 2011, *Baltic Astronomy*, 20, 363
- Allen, M. G., Groves, B. A., Dopita, M. A., Sutherland, R. S., & Kewley, L. J. 2008, *ApJS*, 178, 20
- Baldwin, J. A., Phillips, M. M., & Terlevich, R. 1981, *PASP*, 93, 5
- Bresolin, F., Rizzi, L., Ho, I. T., et al. 2020, *MNRAS*, 495, 4347
- Calzetti, D., Harris, J., Gallagher, John S., I., et al. 2004, *AJ*, 127, 1405
- Cardelli, J. A., Clayton, G. C., & Mathis, J. S. 1989, *ApJ*, 345, 245
- de Blok, W. J. G., Walter, F., Ferguson, A. M. N., et al. 2018, *ApJ*, 865, 26
- Egorov, O. V., Lozinskaya, T. A., & Moiseev, A. V. 2010, *Astronomy Reports*, 54, 277
- Egorov, O. V., Lozinskaya, T. A., Moiseev, A. V., & Smirnov-Pinchukov, G. V. 2014, *MNRAS*, 444, 376
- Egorov, O. V., Lozinskaya, T. A., Moiseev, A. V., & Smirnov-Pinchukov, G. V. 2018, *MNRAS*, 478, 3386
- Epinat, B., Amram, P., Marcelin, M., et al. 2008, *MNRAS*, 388, 500
- Fitzpatrick, E. L. 1999, *PASP*, 111, 63
- Hong, S., Calzetti, D., Gallagher, John S., I., et al. 2013, *ApJ*, 777, 63
- Jones, D. H., Shopbell, P. L., & Bland-Hawthorn, J. 2002, *MNRAS*, 329, 759
- Kaisina, E. I., Makarov, D. I., Karachentsev, I. D., & Kaisin, S. S. 2012, *Astrophysical Bulletin*, 67, 115
- Karachentsev, I. D. & Kaisin, S. S. 2007, *AJ*, 133, 1883
- Karachentsev, I. D., Karachentseva, V. E., & Boerngen, F. 1985, *MNRAS*, 217, 731
- Karachentsev, I. D., Makarov, D. I., & Kaisina, E. I. 2013, *AJ*, 145, 101
- Kauffmann, G., Heckman, T. M., Tremonti, C., et al. 2003, *MNRAS*, 346, 1055
- Kewley, L. J., Dopita, M. A., Sutherland, R. S., Heisler, C. A., & Trevena, J. 2001, *ApJ*, 556, 121
- Kewley, L. J. & Ellison, S. L. 2008, *ApJ*, 681, 1183
- Kewley, L. J., Groves, B., Kauffmann, G., & Heckman, T. 2006, *MNRAS*, 372, 961
- Koleva, M., Prugniel, P., Bouchard, A., & Wu, Y. 2009, *A&A*, 501, 1269
- Kornilov, V., Safonov, B., Kornilov, M., et al. 2014, *PASP*, 126, 482
- Lang, D., Hogg, D. W., Mierle, K., Blanton, M., & Roweis, S. 2010, *AJ*, 139, 1782
- López-Cobá, C., Sánchez, S. F., Bland -Hawthorn, J., et al. 2019, *MNRAS*, 482, 4032
- López-Cobá, C., Sánchez, S. F., Moiseev, A. V., et al. 2017, *MNRAS*, 467, 4951
- Lozinskaya, T. A., Moiseev, A. V., & Podorvanyuk, N. Y. 2003, *Astronomy Letters*, 29, 77
- Makarova, L. N., Grebel, E. K., Karachentsev, I. D., et al. 2002, *A&A*, 396, 473
- Marino, R. A., Rosales-Ortega, F. F., Sánchez, S. F., et al. 2013, *A&A*, 559, A114
- Markwardt, C. B. 2009, in *Astronomical Society of the Pacific Conference Series*, Vol. 411, *Astronomical Data Analysis Software and Systems XVIII*, ed. D. A. Bohlender, D. Durand, & P. Dowler, 251
- Martin, C. L. 1998, *The Astrophysical Journal*, 506, 222
- Moiseev, A. V. 2015, *Astrophysical Bulletin*, 70, 494
- Moiseev, A. V. & Egorov, O. V. 2008, *Astrophysical Bulletin*, 63, 181
- Moiseev, A. V., Perepelitsyn, A. E., & Oparin, D. V. 2020, *Experimental Astronomy*, accepted, DOI: 10.1007/s10686-020-09672-x; arXiv:2005.14598
- Oparin, D. V. & Moiseev, A. V. 2018, *Astrophysical Bulletin*, 73, 298
- Ott, J., Walter, F., & Brinks, E. 2005, *Monthly Notices of the Royal Astronomical Society*, 358, 1453
- Pilyugin, L. S. & Grebel, E. K. 2016, *MNRAS*, 457, 3678
- Pilyugin, L. S., Vílchez, J. M., & Contini, T. 2004, *A&A*, 425, 849
- Sorgho, A., Foster, T., Carignan, C., & Chemin, L. 2019, *MNRAS*, 486, 504
- Storchi-Bergmann, T., Calzetti, D., & Kinney, A. L. 1994, *ApJ*, 429, 572
- Veilleux, S. & Osterbrock, D. E. 1987, *ApJS*, 63, 295
- Walter, F., Brinks, E., de Blok, W. J. G., et al. 2008, *AJ*, 136, 2563
- Walter, F., Weiss, A., Martin, C., & Scoville, N. 2002, *AJ*, 123, 225
- Yun, M. S., Ho, P. T. P., & Lo, K. Y. 1994, *Nature*, 372, 530